Comparison of Energy Stable Simulation of Moving Contact Line Problems using a Thermodynamically Consistent Cahn–Hilliard Navier–Stokes Model

Henning Bonart [†] Christian Kahle [‡] Jens-Uwe Repke [†]

September 20, 2018

Abstract

Liquid droplets sliding along solid surfaces are a frequently observed phenomenon in nature, e.g., raindrops on a leaf, and in everyday situations, e.g., drops of water in a drinking glass. To model this situation, we use a phase field approach, where the bulk model is given by the thermodynamically consistent phase field model from [Abels et al., Math. Mod. Meth. Appl. Sc., 22(3), 2012], while the boundary conditions to model the contact line dynamics are the generalized Navier boundary condition for the fluid and the dynamically advected boundary contact angle condition for the phase field, as derived in [Qian et al., J. Fluid Mech., 564, 2006]. In recent years several schemes were proposed to solve this model numerically. While they widely differ in terms of complexity, they all fulfill certain basic properties when it comes to thermodynamic consistency. However, an accurate comparison of the influence of the schemes on the moving contact line is rarely found. Therefore, we thoughtfully compare the quality of the numerical results obtained with three different schemes and two different free energy potentials. Especially, we discuss the influence of the different schemes on the apparent contact angles of a sliding droplet.

Keywords. Multiphase flows, Drop phenomena, Contact line dynamics, Phase field modeling
AMS subject classification. 35Q30 35Q35 76D05 76M10 76T99

[†]Process Dynamics and Operations Group, Technische Universität Berlin, 10623 Berlin, Germany, {henning.bonart,jens-uwe.repke}@tu-berlin.de

[‡]Center for Mathematical Sciences, Technische Universität München, 85748 Garching bei München, Germany, christian.kahle@ma.tum.de

1 Introduction

Liquid droplets sliding along solid surfaces are a frequently observed phenomenon in nature, e.g., raindrops on a leaf, and in everyday situations, e.g., drops of water in a drinking glass. Furthermore, sliding droplets (and consequently the suppression of those) are crucial in many industrial applications such as coating or painting and separation or reaction processes involving multiple phases and thin liquid films. The position where the interface between the sliding droplet and the surrounding fluid intersects the solid surface is the moving contact line (or contact point if a two dimensional problem is observed). For details about liquids on surfaces and moving contact lines see the reviews [Bonn et al., 2009, Snoeijer and Andreotti, 2013] and the references therein. In a continuum approach, applying the common no-slip boundary condition at the solid surface close to the contact line leads to a non-physical, logarithmically diverging energy dissipation. One possibility to circumvent this difficulty is the coupling of the incompressible Navier–Stokes equations with the Cahn–Hilliard equation [Jacqmin, 2000]. This phase field method models the interface between the fluids with a diffuse interface of positive thickness and describes the distribution of the different fluids by a smooth indicator function. Especially, the Cahn–Hilliard equation allows the contact line to move naturally on the solid surface due to a diffusive flux across the interface, which is driven by the gradient of the chemical potential. Furthermore, the phase field method is able to calculate topological changes like breakup of droplets of merging interfaces [Anderson et al., 1998]. In experiments by e.g., [Carlson et al., 2012, Eddi et al., 2013], it is found that during the rapid spreading of a droplet the contact angle can differ from the equilibrium angle given by Young's equation. To allow for nonequilibrium contact angles, [Jacqmin, 2000] proposes a relaxation of the static contact angle boundary condition, see Section 1.1, and [Qian et al., 2006] extend this approach to include the slip at the contact line stemming from the uncompensated Young stress.

In [Abels et al., 2012] a thermodynamically consistent Cahn–Hilliard Navier–Stokes phase field model is proposed to describe the dynamics of the two phases in the bulk domain. It is valid also for different densities of the involved fluids, but specific contact line dynamics are not included. Recently, several numerical schemes for solving this system have been proposed see e.g., [Garcke et al., 2016, Grün and Klingbeil, 2014, Grün et al., 2016, Aland, 2014, Guillén-Gonzáles and Tierra, 2014, Guillén-González and Tierra, 2013]. All these schemes are thermodynamically consistent in the sense, that they mimic the energy law from [Abels et al., 2012] in the time discrete or even in the fully discrete setting. They range from fully coupled and nonlinear to decoupled and linear, where decoupled means, that the Navier–Stokes and the Cahn–Hilliard equations are solved sequentially.

These schemes are extended to the Cahn–Hilliard Navier–Stokes system with moving contact line in various papers. Here the concepts from the aforementioned papers for the discretization of the bulk equations are straightforwardly used. For the additional contact line boundary conditions typically a stabiliza-

tion approach is used, see e.g., [Aland and Chen, 2016, Yu and Yang, 2017]. We note that a thermodynamically consistent decoupling seems not possible in the presence of the general boundary conditions from [Qian et al., 2006], see e.g., [Aland and Chen, 2016, Yu and Yang, 2017, Grün et al., 2016].

The model from [Abels et al., 2012] contains an additional flux term in the momentum equation, that renders the model thermodynamically consistent. This term is often neglected, see e.g., [Shen and Yang, 2010]. For the resulting model several discretization schemes are proposed and we refer to the references in [Yu and Yang, 2017] for details.

In all these simulations involving moving contact lines a polynomial energy potential is applied. In contrast, we work with a double obstacle potential, which is subsequently relaxed, see [Hintermüller et al., 2011]. In [Garcke et al., 2016] and [Aland et al., 2017] it is shown, that at least in a numerical benchmark setting the results with this kind of energy are typically closer to sharp interface numerics than with the polynomial free energy.

To prepare future research on the passive control of droplets sliding on structured or chemically patterned surfaces, we extend the work of [Garcke et al., 2016] in this paper to the case of moving contact line dynamics and compare the numerical results with the corresponding decoupled scheme from e.g., [Grün et al., 2016] and a fully linear scheme, that both uses decoupling and Eyre's linear scheme [Aland and Chen, 2016]. We test both the polynomially free energy and the relaxed double-obstacle free energy, so that in total we compare six different combinations of energy potentials and solution schemes.

The remainder of the paper is organised as follows. In the second part of the introduction, Section 1.1, we introduce the continuous model as well as the bulk energy potentials and the contact line energies. Afterwards, we derive a weak formulation in Section 2 and the numerical schemes in Section 3. In Section 4.1 we compare the different combinations at first in the bulk without any contact line. Finally, we compare simulation results of sliding droplets on inclined surfaces to investigate the accuracy and efficiency of several linearization and decoupling strategies as well as free energy density formulations for moving contact line problems in Section 4.2. We conclude our work in Section 5.

1.1 Model

In the fluid domain we consider the thermodynamically consistent model for the simulation of two-phase flow presented in [Abels et al., 2012], in the variant for nonlinear density functions proposed in [Abels and Breit, 2016, Eq. 1.10]. To model the contact line dynamics we use generalized Navier boundary conditions for the velocity together with dynamically advected boundary conditions for the phase field as proposed in [Qian et al., 2006].

In strong form the model reads as follows. Let $\Omega \subset \mathbb{R}^d$ with $d \in \{2, 3\}$ denote an open, polygonally/polyhedrally bounded Lipschitz domain and $I = (0, T]$ with $0 < T < \infty$ denote a time interval. The outer unit normal on $\partial\Omega$ is ν_Ω. At time $t \in I$ the primal variables are given by the velocity field v, the pressure field p, the phase field φ and the chemical potential μ. They satisfy the following

system of equations

$$\rho\partial_t v + (\rho v + J)\nabla v + R\frac{v}{2} - \operatorname{div}(2\eta Dv) + \nabla p = -\varphi\nabla\mu + \rho g \qquad \text{in } \Omega, \qquad (1)$$

$$-\operatorname{div}(v) = 0 \qquad \text{in } \Omega, \qquad (2)$$

$$\partial_t\varphi + v\nabla\varphi - b\Delta\mu = 0 \qquad \text{in } \Omega, \qquad (3)$$

$$-\sigma\epsilon\Delta\varphi + \frac{\sigma}{\epsilon}W'(\varphi) = \mu \qquad \text{in } \Omega, \qquad (4)$$

$$v \cdot \nu_\Omega = 0 \qquad \text{on } \partial\Omega, \qquad (5)$$

$$[2\eta Dv\nu_\Omega + l(\varphi)v_{tan} - L(\varphi)\nabla\varphi] \times \nu_\Omega = 0 \qquad \text{on } \partial\Omega, \qquad (6)$$

$$rB + L(\varphi) = 0 \qquad \text{on } \partial\Omega, \qquad (7)$$

$$\nabla\mu \cdot \nu_\Omega = 0 \qquad \text{on } \partial\Omega, \qquad (8)$$

where we abbreviate $J := -b\frac{\partial\rho}{\partial\varphi}\nabla\mu$, $R := -b\nabla\frac{\partial\rho}{\partial\varphi} \cdot \nabla\mu$, $B := \partial_t\varphi + v\nabla\varphi$, $L := \sigma\epsilon\nabla\varphi \cdot \nu_\Omega + \gamma'(\varphi)$. The gravitational acceleration is denoted by g and we abbreviate $2Dv := \nabla v + (\nabla v)^t$. The function $W(\varphi)$ denotes a dimensionless potential of double-well type, with two strict minima at ± 1. We refer to Remark 1 for a discussion of possible choices for W. We formulate (1) with a shifted pressure variable $p = p^{phys} - \mu\varphi$, where p^{phys} denotes the physical pressure.

The contact line energy is denoted by γ, see Remark 2. The constant parameters for the equations in Ω are given by the constant mobility $b > 0$, the scaled surface tension σ, see Remark 1, and the interfacial thickness parameter ϵ. The constant mobility is used for simplicity but the following is also valid for mobilities that depend on φ. The (nonlinear) density function is denoted by $\rho \equiv \rho(\varphi) > 0$ and satisfies $\rho(-1) = \rho_1$ and $\rho(1) = \rho_2$, with ρ_1, ρ_2 denoting the constant densities of the two involved fluids. The (nonlinear) viscosity function is $\eta \equiv \eta(\varphi) > 0$ and satisfies $\eta(-1) = \eta_1$ and $\eta(1) = \eta_2$, with η_1, η_2 denoting the viscosities of the involved fluids. We note, that, while $\int_\Omega \varphi\, dx$ is a conserved quantity, the total mass $\int_\Omega \rho(\varphi)\, dx$ is only conserved if $\rho(\varphi)$ is a linear function on the (a-priori unknown) image of φ, see e.g., [Garcke et al., 2016, Rem. 1].

As boundary data we use generalized Navier boundary conditions for the velocity field and dynamically advected contact angle boundary conditions for the two-phase equation, see [Qian et al., 2006, Eq. 4.4, Eq. 4.5]. Here γ denotes the fluid-solid interfacial free energy, see [Qian et al., 2006, Sec. 4], $l(\varphi)$ is a slip coefficent for the generalized Navier boundary condition applied to the tangential part of the velocity $v_{tan} := v \times \nu_\Omega$, while $L(\varphi)\nabla\varphi \times \nu_\Omega$ is the uncompensated Young stress and L is the chemical potential at the solid surface. The static contact angle is denoted by θ_s and $r \geq 0$ is a phenological parameter allowing for nonequilibrium at the contact line.

Note, that for $r \equiv 0$ (7) reduces to $\sigma\epsilon\nabla\varphi \cdot \nu_\Omega = -\gamma'(\varphi)$, i.e., a static contact angle at the interface is assumed. Furthermore, for $\gamma'(\varphi) \equiv 0$ (or rather $\theta_s \equiv 90°$, see Remark 2), (7) further simplifies to $\nabla\varphi \cdot \nu_\Omega = 0$, which is the no-flux condition for φ at the solid surface. The no-slip condition for v is obtained from (6) by $L \equiv 0$ and $l \to \infty$ (or rather the slip length $l_s \equiv 0$, see Remark 10).

Concerning the existence of solutions to (1) to (5) and (8) together with no-slip for v and a homogeneous Neumann (or no-flux) boundary condition for φ as well as with different assumptions on b and W, we refer to [Abels et al., 2013a, Abels et al., 2013b, Abels and Breit, 2016, Grün, 2013]. For the boundary conditions considered here we are not aware of such results, but refer to [Colli et al., 2017] for analytical results for the Cahn–Hilliard system with dynamic boundary conditions and to [Grün et al., 2016] for a Cahn–Hilliard Navier–Stokes model with dynamical contact angle condition, but no-slip condition for the Navier–Stokes equation.

For (1) to (5) and (8) together with no-slip for v and no-flux for φ, several thermodynamically consistent discretization schemes were proposed in the last years. Here, we refer to [Guillén-Gonzáles and Tierra, 2014, Grün and Klingbeil, 2014, Garcke et al., 2016]. Especially in [Garcke et al., 2016] the influence of spatial adaptivity on the fully discrete energy law is discussed. We further refer to [Aland, 2014], where the benefit of using fully coupled schemes is shown numerically, and to [Guillén-González and Tierra, 2013] for a extensive discussion of several discretization schemes for the potential W^{poly}.

For the full model (1)–(8) thermodynamically consistent schemes are e.g., proposed in [Aland and Chen, 2016] for the case of constant density, and in [Yu and Yang, 2017] for the general case. The case with no-slip boundary condition for v and dynamically advected boundary condition for φ is numerically and analytically considered in [Grün et al., 2016].

Remark 1 (Potentials W)**.** *Throughout this work we consider polynomially bounded potentials for W. To state the precise assumptions we split $W = W_+ + W_-$ with W_+ denoting the convex part of W and W_- denoting the concave part. We assume that $W : \mathbb{R} \to \mathbb{R}$ is continuously differentiable and that W and its derivatives W'_+ and W'_- are polynomially bounded, i.e., there exists $C > 0$ such that*

$$|W(\varphi)| \leq C(1 + |\varphi|^4), \quad |W'_+(\varphi)| \leq C(1 + |\varphi|^3), \quad |W'_-(\varphi)| \leq C(1 + |\varphi|^3).$$

Note that these bounds on the polynomial degree might be relaxed, see [Garcke et al., 2016, (A3)] and that these assumptions are used to show the existence of discrete solutions.

These assumptions are for example fulfilled by the commonly used polynomial potential

$$W^{poly}(\varphi) := \frac{1}{4}(1 - \varphi^2)^2, \quad W^{poly_2}(\varphi) := \begin{cases} \frac{1}{4}(1 - \varphi^2)^2 & \text{if } |\varphi| \leq 1, \\ (|\varphi| - 1)^2 & \text{else,} \end{cases}$$

where W^{poly_2} is a modification of W^{poly} that guarantees an L^∞ bound on φ, see [Caffarelli and Muler, 1995].

Another potential that fulfills the assumptions is

$$W^s(\varphi) := \frac{1}{2}\left(1 - (\xi\varphi)^2 + s\lambda(\xi\varphi)^2\right) + \theta,$$

where $\lambda(x) := \max(0, x-1) + \min(0, x+1)$, *and* $\theta := \frac{1}{2(s-1)}$ *and* $\xi := \frac{s}{s-1}$ *are chosen such, that* $W(\pm 1) \equiv 0$ *are the two minima of* W^s. *Here* $s \gg 0$ *is a penalisation parameter. We typically experience better results in the sense of sharper interfaces with this potential. It appears as Moreau–Yosida relaxation of the double obstacle potential* W^∞, *see [Blowey and Elliott, 1991, Hintermüller et al., 2011]. In a synthetic rising bubble benchmark, see [Hysing et al., 2009], our results with this potential are typically closer to the results from sharp interface methods then with the potential* W^{poly}, *see [Garcke et al., 2016, Tab. 1].*

In the following, whenever we use the letter W, *we mean any of the three mentioned potentials.*

For preparation of later results, let us state the splittings of W *into* $W(\varphi) = W_+(\varphi) + W_-(\varphi)$. *These splittings are*

$$W_+^{poly}(\varphi) = \frac{1}{4}\varphi^4 + \frac{1}{4}, \qquad W_-^{poly}(\varphi) = -\frac{1}{2}\varphi^2,$$

$$W_+^{poly_2}(\varphi) = \begin{cases} \varphi^2 + \varphi + \frac{1}{2} & \text{if } \varphi < -1, \\ \frac{1}{4}\varphi^4 + \frac{1}{4} & \text{if } |\varphi| \le 1, \\ \varphi^2 - \varphi + \frac{1}{2} & \text{if } \varphi > 1, \end{cases} \quad W_-^{poly_2}(\varphi) = \begin{cases} \varphi + \frac{1}{2} & \text{if } \varphi < -1, \\ -\frac{1}{2}\varphi^2 & \text{if } |\varphi| \le 1, \\ -\varphi + \frac{1}{2} & \text{if } \varphi > 1, \end{cases}$$

$$W_+^s(\varphi) = \frac{s}{2}\lambda(\xi\varphi)^2 + \theta, \qquad W_-^s(\varphi) = \frac{1}{2}(1 - (\xi\varphi)^2).$$

To define the scaled surface tension σ *we introduce the constant* c_W *as* $c_W^{-1} = \int_{-\infty}^{\infty} 2W(\Phi_0(z))\,dz = \int_{-\infty}^{\infty} (\partial_z \Phi_0(z))^2\,dz$, *where* Φ_0 *denotes the first order approximation of* φ *depending on* W, *see e.g., [Abels et al., 2012, 4.3.3]. Then* $\sigma = c_W \sigma_{12}$, *where* σ_{12} *denotes the physical value of the surface tension between the phases* 1 *and* 2.

Using W^{poly} *and* W^{poly_2} *we obtain* $c_W = \frac{3}{2\sqrt{2}}$, *and using the relaxed double obstacle potential* W^s *we calculate*

$$c_W^{-1} = (1 - s^{-2}) \arctan(\sqrt{s-1}) + s^{-2}(s+2)\sqrt{s-1}.$$

Especially for $s \to \infty$ *we recover the well-known scaling* $c_W = \frac{2}{\pi}$ *for the double-obstacle potential.*

Remark 2 (Contact line energy)**.** *The basic formula to derive the contact line energy is given by Young's law, namely*

$$\sigma_{s1} - \sigma_{s2} = \sigma_{12} \cos\theta_s.$$

Here σ_{s1} *and* σ_{s2} *denote the physical surface tensions between the phase 1 (*$\varphi = -1$*) and the solid (*σ_{s1}*) and phase 2 (*$\varphi = 1$*) and the solid (*σ_{s2}*). Further* σ_{12} *denotes the surface tension between phase 1 and 2 and* θ_s *denotes the static equillibrium contact angle between the solid and the interface and is measured in phase 2.*

We use the ansatz

$$\gamma(\varphi) := \frac{\sigma_{s1} + \sigma_{s2}}{2} - \sigma_{12} \cos\theta_s \vartheta(\varphi)$$

and choose $\vartheta(\varphi)$ to fulfill

$$\gamma(-1) = \sigma_{s1}, \quad \gamma(0) = \frac{\sigma_{s1} + \sigma_{s2}}{2}, \quad \gamma(1) = \sigma_{s2}, \quad \gamma'(\pm 1) = 0.$$

Especially $\vartheta(-1) = -\frac{1}{2}$ and $\vartheta(1) = \frac{1}{2}$ holds. Note that here the unscaled values for the surface tensions appear as can be shown by matched asymptotic expansions as in [Abels et al., 2012, Sec. 4.3.4].

One possibility is to choose $\vartheta^{\sin}(\varphi) := \frac{1}{2}\sin(\frac{\pi}{2}\varphi)$ as proposed in [Qian et al., 2006, Sec. 4].

An alternative is given in [Ding and Spelt, 2007]. Here the assumption of equipartition of energy, i.e., $\frac{\epsilon}{2}|\nabla\varphi|^2 \approx \frac{1}{\epsilon}W(\varphi)$ is used to derive $(\vartheta^W)'(\varphi) = c_W\sqrt{2W(\varphi)}$.

Finally, we state a contact line energy, that allows for a convex-concave splitting, namely $\vartheta^{cc}(\varphi) = \vartheta^{cc}_+(\varphi) + \vartheta^{cc}_-(\varphi)$ with

$$\vartheta^{cc}_+(\varphi) = \begin{cases} -\frac{1}{2} & \text{if } \varphi \le -1, \\ \frac{1}{2}(\varphi+1)^2 - \frac{1}{2} & \text{if } \varphi \in (-1,0), \\ \varphi & \text{if } \varphi \ge 0, \end{cases} \quad \vartheta^{cc}_-(\varphi) = \begin{cases} 0 & \text{if } \varphi \le 0, \\ -\frac{1}{2}\varphi^2 & \text{if } \varphi \in (0,1), \\ \frac{1}{2} - \varphi & \text{if } \varphi \ge 1. \end{cases}$$

Here ϑ^{cc}_+ is convex and ϑ^{cc}_- is concave and $\vartheta^{cc} \in C^{1,1}(\mathbb{R})$ with $\vartheta'' \in L^\infty(\mathbb{R})$.

Note that for any ϑ that has a bounded second derivative, we can define a convex-concave splitting via

$$\vartheta_+(\varphi) = \vartheta(\varphi) + \frac{1}{2}\max_{\phi\in\mathbb{R}}(\vartheta''(\phi))\varphi^2, \qquad \vartheta_-(\varphi) = -\frac{1}{2}\max_{\phi\in\mathbb{R}}(\vartheta''(\phi))\varphi^2,$$

compare [Backofen et al., 2018]. This is very similar to the stabilization approach, proposed e.g., [Aland and Chen, 2016], that essentially resembles one of Eyre's linear schemes [Guillén-González and Tierra, 2013]. In the following we always assume a convex-concave splitting of γ.

2 The weak formulation

We next derive the weak formulation that is the basis for our numerical scheme that we propose in Section 3. For this we assume sufficient regularity of all appearing functions. Multiplying (3) with $\frac{\partial\rho}{\partial\varphi}$ we observe

$$\partial_t\rho + \operatorname{div}(\rho v + J) = R. \tag{9}$$

Note that if ρ is a nonlinear function $R \neq 0$ holds and thus mass conservation can be violated as soon as a nonlinear function for ρ is used to guarantee $\rho > 0$. Note that the conservation of φ is not affected. Using (9) the momentum equation (1) can equivalently be written as

$$\partial_t(\rho v) + \operatorname{div}\left(v \otimes (\rho v + J)\right) - R\frac{v}{2} - \operatorname{div}\left(2\eta Dv\right) + \nabla p = -\varphi\nabla\mu + \rho g, \tag{10}$$

see [Abels and Breit, 2016, (1.12)]. We stress that this reformulation is independent of the actual boundary condition.

To define the weak formulation we multiply both (1) and (10) by a solenoidal test function $\frac{1}{2}w$ that satisfies $w|_{\partial\Omega}\cdot\nu_\Omega = 0$ and sum up the equations to achieve

$$\begin{aligned}&\frac{1}{2}\int_\Omega(\rho\partial_t v+\partial_t(\rho v))w\,dx-\int_\Omega \operatorname{div}(2\eta Dv)\,w\,dx\\ &+\frac{1}{2}\int_\Omega((\rho v+J)\nabla)vw\,dx+\frac{1}{2}\int_\Omega \operatorname{div}(v\otimes(\rho v+J))\,w\,dx=\int_\Omega -\varphi\nabla\mu+\rho g\,dx.\end{aligned}\tag{11}$$

Using integration by parts together with the boundary conditions $v\cdot\nu_\Omega = 0$ and $\nabla\mu\cdot\nu_\Omega = 0$ we observe

$$\begin{aligned}&\frac{1}{2}\int_\Omega((\rho v+J)\nabla)vw\,dx+\frac{1}{2}\int_\Omega \operatorname{div}(v\otimes(\rho v+J))\,w\,dx &(12)\\ =&\frac{1}{2}\int_\Omega((\rho v+J)\nabla)vw-((\rho v+J)\nabla)wv\,dx &(13)\\ =:&a(\rho v+J,v,w). &(14)\end{aligned}$$

Note that $a(\cdot,v,v)=0$ holds. Using integration by parts for the viscous stress we observe

$$\begin{aligned}-\int_\Omega \operatorname{div}(2\eta Dv)\,w\,dx&=\int_\Omega 2\eta Dv:Dw\,dx-\int_{\partial\Omega}2\eta Dv\nu_\Omega w\,ds, &(15)\\ &=\int_\Omega 2\eta Dv:Dw\,dx+\int_{\partial\Omega}(l(\varphi)v_{tan}+rB\nabla\varphi)w\,ds &(16)\end{aligned}$$

where $Dv:Dw:=\sum_{ij=1}^n(Dv)_{ij}(Dw)_{ij}$ and we use the boundary conditions (6) and (7).

The weak form of (3)–(4) is derived by the standard procedure and summarizing we obtain the following weak form of (1)–(8):

Definition 3 (The weak formulation)**.** *Find sufficiently smooth v,μ,φ, with v solenoidal, $v\cdot\nu_\Omega=0$, such that for all w, ψ, ϕ, with w solenoidal the following equations are satisfied:*

$$\begin{aligned}&\frac{1}{2}\int_\Omega(\rho\partial_t v+\partial_t(\rho v))w\,dx+a(\rho v+J,v,w)+\int_\Omega 2\eta Dv:Dw\,dx\\ &+\int_{\partial\Omega}(l(\varphi)v_{tan}+rB(\varphi_t,\varphi,v)\nabla\varphi)w\,ds-\int_\Omega(-\varphi\nabla\mu+\rho g)w\,dx=0, &(17)\\ &\int_\Omega\varphi_t\psi\,dx-\int_\Omega\varphi v\cdot\nabla\psi\,dx+\int_\Omega b\nabla\mu\cdot\nabla\psi\,dx=0, &(18)\\ &\int_\Omega\sigma\epsilon\nabla\varphi\cdot\nabla\phi+\frac{\sigma}{\epsilon}W'(\varphi)\phi\,dx-\int_\Omega\mu\phi\,dx\\ &+\int_{\partial\Omega}(rB(\varphi_t,\varphi,v)+\gamma'(\varphi))\,\phi\,ds=0. &(19)\end{aligned}$$

The weak form (17)–(19) allows us to derive the following energy identity.

Theorem 4 (The formal energy identity)**.** *Assume there exists a sufficiently smooth solution to* (17)–(19)*. Then the following energy identity holds.*

$$\begin{aligned}\frac{d}{dt}\left(\int_\Omega \frac{1}{2}\rho|v|^2\,dx + \sigma\int_\Omega \frac{\epsilon}{2}|\nabla\varphi|^2 + \frac{1}{\epsilon}W(\varphi)\,dx + \int_{\partial\Omega}\gamma\,ds\right)\\ + \int_\Omega 2\eta|Dv|^2\,dx + \int_\Omega b|\nabla\mu|^2\,dx \qquad (20)\\ + \int_{\partial\Omega} l(\varphi)|v_{tan}|^2\,ds + r\int_{\partial\Omega}|B(\varphi_t,\varphi,v)|^2\,ds = \int_\Omega \rho g v\,dx.\end{aligned}$$

Note that the energy in the system can only be increased by the gravitational acceleration.

Proof. Use $w \equiv v$, $\Psi \equiv \mu$, and $\Phi \equiv \partial_t\varphi$ as test functions in (17)–(19) and sum up the resulting equation. □

3 The numerical schemes

For a practical implementation in a finite element scheme we introduce a time grid $0 = t_0 < t_1 < \ldots < t_{m-1} < t_m < \ldots < t_M = T$ on $I = [0,T]$. Due to notational simplicity let the time grid be equidistant with step size $\tau > 0$. We further introduce a triangulation $\mathcal{T}_h$ of $\overline{\Omega}$ into cells T_i, such that $\mathcal{T}_h = \bigcup_{i=1}^N T_i$ covers $\overline{\Omega}$ exactly.

On $\mathcal{T}_h$ we introduce the finite element spaces

$$\begin{aligned}V_1 &:= \{v \in C(\overline{\Omega}) \,|\, v|_{T_i} \in \mathcal{P}_1\},\\ V_2 &:= \{v \in C(\overline{\Omega})^d \,|\, v|_{T_i} \in (\mathcal{P}_2)^2,\, v\cdot\nu_\Omega = 0\},\end{aligned}$$

where $\mathcal{P}_k$ denotes the space of polynomials of order up to k.

We use V_1 to define discrete approximation φ_h, μ_h, and p_h of the corresponding continous variables, and V_2 to define the discrete approximation v_h of v. This means, that we use standard Taylor–Hood elements for the Navier–Stokes part and explicitly denote the pressure variable in the following.

The scheme reads as follows:
Given $\varphi^{m-1} \in V_1$, $\mu^{m-1} \in V_1$, and $v^{m-1} \in V_2$, find $\varphi_h^m \in V_1$, $\mu_h^m \in V_1$, $p_h^m \in V_1$ and $v_h^m \in V_2$, such that for all $w \in V_2$, $q \in V_1$, $\Phi \in V_1$, and $\Psi \in V_1$ the following

equations hold

$$\begin{aligned}
\frac{1}{\tau}\left(\frac{\rho^m+\rho^{m-1}}{2}v_h^m-\rho^{m-1}v^{m-1},w\right)\\
+a(\rho^{m-1}v^{m-1}+J^{m-1},v_h^m,w)+(2\eta^{m-1}Dv_h^m,Dw)-(\mathrm{div}w,p_h^m)\\
+(l(\varphi^{m-1})v_{h,tan}^m+rB_h^m\nabla\varphi^{m-1},w)_{\partial\Omega}\\
+(\varphi^{m-1}\nabla\mu_h^m,w)-(g\rho^{m-1},w)=0, \quad (21)\\
-(\mathrm{div}v_h^m,q)=0, \quad (22)\\
\frac{1}{\tau}(\varphi_h^m-\varphi^{m-1},\Psi)-(\varphi^{m-1}v_h^m,\nabla\Psi)+(b\nabla\mu_h^m,\nabla\Psi)=0, \quad (23)\\
\sigma\epsilon(\nabla\varphi_h^m,\nabla\Phi)+\frac{\sigma}{\epsilon}(W_+'(\varphi_h^m)+W_-'(\varphi^{m-1}),\Phi)-(\mu_h^m,\Phi)\\
+(rB_h^m,\Phi)_{\partial\Omega}+\left(\gamma_+'(\varphi^m)+\gamma_-'(\varphi^{m-1}),\Phi\right)_{\partial\Omega}=0, \quad (24)
\end{aligned}$$

with $J^{m-1}:=-b\frac{\partial\rho}{\partial\varphi}(\varphi^{m-1})\nabla\mu^{m-1}$, $B_h^m:=\left(\frac{\varphi_h^m-\varphi^{m-1}}{\tau}+v_h^m\nabla\varphi^{m-1}\right)$, $\rho^{m-1}:=\rho(\varphi^{m-1})$, and $\eta^{m-1}:=\eta(\varphi^{m-1})$.

Using Brouwer's fixed-point theorem one can show the existence of at least one solution following [Garcke et al., 2016, Thm. 2]. The uniqueness stays unclear due to the nonlinearity $\rho^m v_h^m$ in (21).

The scheme fulfills a fully discrete variant of the formal energy identity (20).

Theorem 5 (The fully discrete energy inequality)**.** *Let $\varphi_h^m\in V_1^m$, $\mu_h^m\in V_1^m$, and $v_h^m\in V_2^m$ denote a solution to* (21)–(24)*. Then the following energy inequality holds*

$$\begin{aligned}
\frac{1}{\tau}\left(\frac{1}{2}\int_\Omega\rho^m|v_h^m|^2+\sigma\int_\Omega\frac{\epsilon}{2}|\nabla\varphi_h^m|^2+\frac{1}{\epsilon}W(\varphi_h^m)\,dx+\int_{\partial\Omega}\gamma(\varphi_h^m)\,ds\right)\\
+\int_\Omega 2\eta^{m-1}|Dv_h^m|^2\,dx+b\int_\Omega|\nabla\mu_h^m|^2\,dx+\int_{\partial\Omega}l(\varphi^{m-1})|v_{h,tan}^m|^2\,ds+r\int_{\partial\Omega}|B_h^m|^2\,ds\\
+\frac{1}{\tau}\left(\frac{1}{2}\int_\Omega\rho^{m-1}|v_h^m-v^{m-1}|^2\,dx+\frac{\sigma\epsilon}{2}\int_\Omega|\nabla\varphi_h^m-\nabla\varphi^{m-1}|^2\,dx\right)\\
\le\frac{1}{\tau}\left(\frac{1}{2}\int_\Omega\rho^{m-1}|v^{m-1}|^2+\sigma\int_\Omega\frac{\epsilon}{2}|\nabla\varphi^{m-1}|^2+\frac{1}{\epsilon}W(\varphi^{m-1})\,dx+\int_{\partial\Omega}\gamma(\varphi^{m-1})\,ds\right)\\
+\int_\Omega\rho^{m-1}g\cdot v_h^m\,dx. \qquad (25)
\end{aligned}$$

Proof. We use $w\equiv v_h^m$, $\Psi\equiv\mu_h^m$ and $\Phi\equiv\frac{\varphi_h^m-\varphi_h^{m-1}}{\tau}$ as test functions in (21)–

(24) and sum up to obtain

$$\begin{aligned}
\frac{1}{\tau}\left(\frac{1}{2}\int_\Omega \rho^m|v_h^m|^2 - \frac{1}{2}\int_\Omega \rho^{m-1}|v_h^{m-1}|^2 + \frac{1}{2}\int_\Omega \rho^{m-1}|v_h^m - v^{m-1}|^2\,dx\right)& \\
+\int_\Omega 2\eta^{m-1}|Dv_h^m|^2\,dx - \int_\Omega \rho^{m-1} g\cdot v_h^m\,dx& \\
+\int_{\partial\Omega} l(\varphi^{m-1})v_{h,tan}^m v_h^m\,ds + r\int_{\partial\Omega} B_h^m \nabla\varphi_h^{m-1}\cdot v_h^m\,ds& \\
+b\int_\Omega |\nabla\mu_h^m|^2\,dx& \\
+\frac{\sigma\epsilon}{2\tau}\left(\int_\Omega |\nabla\varphi_h^m|^2 - |\nabla\varphi_h^{m-1}|^2 + |\nabla\varphi_h^m - \nabla\varphi^{m-1}|^2\,dx\right)& \\
+\frac{\sigma}{\epsilon}\int_\Omega (W_+'(\varphi_h^m) + W_-'(\varphi^{m-1}))\frac{\varphi_h^m - \varphi^{m-1}}{\tau}\,dx& \\
+r\int_{\partial\Omega} B_h^m\frac{\varphi_h^m - \varphi^{m-1}}{\tau}\,ds + \int_{\partial\Omega}(\gamma_+'(\varphi_h^m) + \gamma_-'(\varphi^{m-1}))\frac{\varphi_h^m - \varphi^{m-1}}{\tau}\,ds = 0.&
\end{aligned}$$

Using convexity and concavity of W_+ and W_-, and γ_+ and γ_- it holds

$$\begin{aligned}
\int_\Omega (W_+'(\varphi_h^m) + W_-'(\varphi^{m-1}))\frac{\varphi_h^m - \varphi^{m-1}}{\tau}\,dx &\geq \frac{1}{\tau}\int_\Omega W(\varphi_h^m) - W(\varphi^{m-1})\,dx,\\
\int_\Omega (\gamma_+'(\varphi_h^m) + \gamma_-'(\varphi^{m-1}))\frac{\varphi_h^m - \varphi^{m-1}}{\tau}\,ds &\geq \frac{1}{\tau}\int_\Omega \gamma(\varphi_h^m) - \gamma(\varphi^{m-1})\,ds.
\end{aligned}$$

Summing up and using $v\cdot\nu_\Omega = 0$ we obtain the desired result. □

Remark 6. *In general, in diffuse interface simulations it is advantageous to use adaptive meshes to resolve the interfacial region. Then in every time step additional prolongation operators between subsequent meshes are required. As a consequence, in this case the energy inequality from Theorem 5 only holds with the prolongated data for the energy from the old time instance. We further note, that special care has to be taken for prolongating the velocity field, as the prolongated velocity field typically is not solenoidal with respect to the new mesh. We refer to [Garcke et al., 2016] for further discussion of this topic.*

3.1 Variants

Let us state variants of the above discretization scheme (21)–(24) for numerical comparison. We note, that (21)–(24) is a fully coupled and non-linear scheme.

3.1.1 A stable decoupled scheme

If $r \equiv 0$ the scheme is only coupled by the transport term $(\varphi^{m-1}v_h^m, \nabla\Psi)$ in (23). The same holds for $l \to \infty$, which results in commonly used no-slip conditions for the Navier–Stokes equation. In the case of no-slip conditions B

is independent of v and thus again the only coupling is the transport term in (23).

In both cases we can decouple the Navier–Stokes equation and the Cahn–Hilliard equation by using an augmented velocity field in (23), see for example [Minjeaud, 2013, Guillén-Gonzáles and Tierra, 2014, Grün et al., 2016, Yu and Yang, 2017]. Here we substitute $-\int_\Omega \varphi^{m-1} v_h^m, \nabla\Psi\, dx$ in (23) by

$$-\int_\Omega \varphi^{m-1} v^{m-1} \nabla\Psi\, dx + \tau \int_\Omega (\rho^{m-1})^{-1} |\varphi^{m-1}|^2 \nabla \mu_m^h \cdot \nabla\Psi\, dx. \tag{26}$$

The resulting scheme is now decoupled, i.e., we can first solve (23) and (24) and thereafter (21) and (22). This scheme is also energy stable, as the additional integral compensates terms arising from Hölder's and Young's inequality to balance the first integral with the numerical dissipation $\frac{1}{2}\int_\Omega \rho^{m-1}|v_h^m - v^{m-1}|^2\, dx$. This scheme with no-slip conditions for Navier–Stokes and $r \equiv 0$ is analyzed in [Grün et al., 2016] for different treatments of W'. We also refer to [Kay et al., 2008] for an alternative decoupling in the case of constant density. Here the systems are decoupled by only using v^{m-1} in (23), and the energy stability is obtained by introducing a step size restriction for the temporal discretization.

If $r > 0$ we use v^{m-1} in the definition of B_h^m in (24) and v_h^m in the corresponding term in (21) and can still derive an energy inequality containing an error of order $r\int_{\partial\Omega}(v_h^m - v^{m-1}) \cdot \nabla\varphi^{m-1}\, ds$. In [Grün et al., 2016] a no slip condition is assumed for v to decouple the boundary conditions. Then the decoupling proposed in (26) is sufficient to decouple the Navier–Stokes and the Cahn–Hilliard equation.

We note that this scheme can be applied for any free energy density that admits a convex-concave splitting.

3.1.2 A stable decoupled and linear scheme

Using the decoupling proposed in Section 3.1.1, the only nonlinearity in the scheme arises from W_+'. In [Aland and Chen, 2016, Yu and Yang, 2017], a stabilized linear scheme is used and the term $W_+'(\varphi_h^m) + W_-'(\varphi^{m-1})$ is substituted by $W'(\varphi^{m-1}) + S_W(\varphi_h^m - \varphi^{m-1})$, where S_W is a suitable stabilization parameter, which is of order W''. If we use W^s as free energy density, it has to be chosen like $S_W \in \mathcal{O}(s)$. For large values of $s \gg 0$ we expect that this stabilization will prevent changes in φ_h and thus might have a deep impact on the allover dynamics. This is investigated in Section 4.

To linearize γ we substitute $\gamma_+'(\varphi_h^m) + \gamma_-'(\varphi^{m-1})$ by $\gamma'(\varphi_h^{m-1}) + S_\gamma(\varphi_h^m - \varphi^{m-1})$ with $S_\gamma \equiv \frac{1}{2}\sigma_{12}\cos(\theta_s)$.

Remark 7. *For further discretization schemes for the free energy density W we refer for example to [Guillén-González and Tierra, 2013, Grün et al., 2016]. We note that most schemes are not applicable for the free energy density W^s, as high regularity is required.*

Remark 8. *Considering the energy inequality* (25) *the terms in the first line correspond to the discrete energy of the system, while the second line corresponds to the energy dissipation of the system, and the third line corresponds to numerical dissipation of the scheme. Thus we call a scheme thermodynamically consistent, if the inequality* (25) *without the numerical dissipation is fullfilled, i.e., if*

$$\begin{aligned}
&\frac{1}{2}\int_\Omega \rho^m |v_h^m|^2 + \sigma \int_\Omega \frac{\epsilon}{2}|\nabla \varphi_h^m|^2 + \frac{1}{\epsilon} W(\varphi_h^m)\,dx + \int_{\partial\Omega} \gamma(\varphi_h^m)\,ds \\
&\qquad + \tau \int_\Omega 2\eta^{m-1}|Dv_h^m|^2\,dx + \tau \int_\Omega b|\nabla \mu_h^m|^2\,dx \\
&\qquad + \tau \int_{\partial\Omega} l(\varphi^{m-1})|v_{h,tan}^m|^2\,ds + \tau \int_{\partial\Omega} r|B_h^m|^2\,ds \\
\leq\ &\frac{1}{2}\int_\Omega \rho^{m-1}|v^{m-1}|^2 + \sigma \int_\Omega \frac{\epsilon}{2}|\nabla \varphi^{m-1}|^2 + \frac{1}{\epsilon} W(\varphi^{m-1})\,dx + \int_{\partial\Omega} \gamma(\varphi^{m-1})\,ds \\
&\qquad + \tau \int_\Omega \rho^{m-1} g \cdot v_h^m\,dx,
\end{aligned} \tag{27}$$

holds. We investigate this energy inequality numerically in Section 4. Note that in contrast to (20) *an inequality appears due to the time discretization of the non-linear potential* W.

4 Numerics

In this section we investigate the three schemes under consideration numerically. In Section 4.1 we briefly give results from the second benchmark in [Hysing et al., 2009], where no contact line motion is included, to estimate the difference of the schemes in the bulk. In Section 4.2 we thereafter investigate the behaviour of the contact line for a gravity-driven droplet sliding on an inclined surface.

We implement the schemes using FEniCS 2017.2.0 [Alnæs et al., 2015, Logg et al., 2012] together with the PETSc 3.8.4 [Balay et al., 2018a, Balay et al., 2018b, Balay et al., 1997] linear algebra backend. Linear systems are solved in parallel using MUMPS 5.1.1 [Amestoy et al., 2001, Amestoy et al., 2006].

4.1 Rising Bubble

At first, we discuss the accuracy of the proposed schemes without moving contact lines. Later on, this allows for an evaluation of the influence of the schemes on the moving contact line. Therefore, we employ the quantitative benchmark case proposed in [Hysing et al., 2009]. In [Aland and Voigt, 2012] it is found, that three different diffuse interface approximations together with the polynomial potential W^{poly} agree well with the sharp interface results from [Hysing et al., 2009]. In [Garcke et al., 2016] the benchmark is used to compare to a phase field model with a relax double obstacle potential.

4.1.1 Setup

Table 1 lists the properties of our simulations, which correspond to the second benchmark case in [Hysing et al., 2009]. For details on the setup we refer to the mentioned references above. Note, that σ_{12} denotes the physical surface tension, yielding $\sigma \approx 1.24$ for W^s. Following [Hysing et al., 2009], we introduce a characteristic length scale $L = 2r_0$, where r_0 is equals the initial radius of the bubble, and a characteristic velocity scale $U = \sqrt{Lg}$. To classify our simulations we indicate in Table 1 the dimensionless numbers Reynolds $Re = \frac{\rho_l U L}{\eta_l}$, Eötvös (or Bond) $Eo = \frac{\rho_l g L^2}{\sigma}$, Capillary $Ca = \frac{\eta_l U}{\sigma}$, Atwood $A = \frac{\rho_l - \rho_g}{\rho_l + \rho_g}$, Cahn $Cn = \frac{\epsilon}{L}$ and Péclet $Pe = \frac{LU\epsilon}{b\sigma}$, see [Khatavkar et al., 2006].

We apply no-slip boundary conditions for the velocity on the top and bottom walls, free-slip on the left and symmetry at the centerline through the bubble at $x = 0.5$. Similar to [Garcke et al., 2016], we set $b = 10^{-3}\epsilon$ and $\epsilon = 0.02$. The time discretization step is chosen as $\tau = 5 \times 10^{-5}$ and the final time is $t = 3$. We initialized the simulations by solving the Cahn–Hilliard equations without convection until a steady state is reached. In total, we perform 7 distinct simulations using the three schemes from Section 3 with W^{poly2} and W^s with $s = 100$, and one additional simulation with $s = 10$ for the fully linear and stabilized scheme with W^s, see the first three columns in Table 2.

In [Hysing et al., 2009] a set of benchmark parameters is defined, that we define in the phase field setting as follows.

The center of mass is calculated using

$$(x_c, y_c) = \frac{\int_\Omega (x, y) \frac{1+\varphi}{2}\, dx}{\int_\Omega \frac{1+\varphi}{2}\, dx}\,, \tag{28}$$

where $\frac{1+\varphi}{2} \equiv 1$ is an indicator for the droplet.

We define the mean velocity in unit direction $a \in \mathbb{R}^2$ as

$$v_a = \frac{\int_\Omega v \cdot a \frac{1+\varphi}{2}\, dx}{\int_\Omega \frac{1+\varphi}{2}\, dx}\,. \tag{29}$$

If a denotes the unit vector in rising direction, this is called rising velocity v_r, while if a points in sliding direction, we call this value sliding velocity v_s.

Finally we define the stretching of the interface as

$$c = \frac{c_W \int_\Omega (\frac{\epsilon}{2}|\nabla\varphi_0|^2 + \frac{1}{\epsilon}W(\varphi_0))\, dx}{c_W \int_\Omega (\frac{\epsilon}{2}|\nabla\varphi|^2 + \frac{1}{\epsilon}W(\varphi))\, dx}\,. \tag{30}$$

Here the denominator denotes an approximation to the length of the interface represented by φ, and the numerator denotes the same for the initial phase field φ_0. If φ_0 denotes a sphere, this is equivalent to the circularity as defined in [Hysing et al., 2009] as the volume of the bubble is constant over time.

Remark 9 (Choice of s in W^s)**.** *For the choice of the relaxation parameter s in W^s, see Remark 1, several points must be considered. To reduce the intermixing between the phases and increase the rate at which the equilibrium profile*

σ_{12}	ρ_l	ρ_g	η_l	η_g	g_y	Re	Eo	Ca	A
1.96	1000	1	10	0.1	-0.98	35	125	3.5	0.99
ϵ	b	τ	$h_{\min}$			Cn	Pe		
2×10^{-2}	2×10^{-5}	5×10^{-5}	0.00625			0.04	178		

Table 1: Parameters used in the rising bubble simulations.

of φ is reestablished after a deformation, it is desirable to exhibit a large spinodal region and subsequently a small metastable region [Donaldson et al., 2011]. The metastable region of the potential W^s is located between $1 > |\varphi| > \xi^{-1} = 1 - \frac{1}{s}$. Thus, to obtain a small metastable region a large value for s is desirable. Furthermore, referring to [Garcke et al., 2016, Kahle, 2017], the value of s controls the deviation of the L^∞ norm of φ from 1. Since ρ and η directly depend on φ a small deviation is desirable, which is achieved by a large value of s.

On the other hand, the stable decoupled and linear scheme, Section 3.1.2, includes a stabilization parameter S_W which has to be chosen like $\mathcal{O}(s)$ for W^s. In this case a large value of s has a severe impact on the overall dynamics as the stabilization can be interpreted as adding the quadratic potential $\frac{S_W}{2}\|\varphi - \varphi^{m-1}\|^2$ to W for given φ^{m-1}. For large values of S_W thus $\varphi \equiv \varphi^{m-1}$ is preferred. To show the influence of S_W in the case $W \equiv W^s$ we test the linear and decoupled scheme with two values of s.

4.1.2 Results

The resulting benchmark values are listed in Table 2. As it is not even clear in the sharp interface simulations whether or not topological changes develop, e.g., the separation of trailing gas filaments, we follow [Aland and Voigt, 2012] and compare our results only up to this time instance ($t = 2$). It is evident, that all the schemes give very similar results compared to the sharp interface solution. Especially we observe, that decoupling the two systems only has a very small impact on the benchmark values in both cases. Further, as expected, we observe a stronger impact of the linear scheme when using W^s then with W^{poly_2}, and this is stronger for larger values of s.

4.2 Sliding Droplet

To compare the influence of the numerical schemes from Section 3 on the moving contact line, simulations of single droplets sliding down an inclined surface are performed. Besides the effect of gravity on the droplet movement, this test case allows to observe both an advancing and receding contact line.

Bulk potential	Decoupled?	Linear?	y_c	$v_{\max}$	$t_{v_{\max}}$	$c_{\min}$	$t_{c_{\min}}$
$W^{s=100}$	no	no	0.9059	0.2475	0.7349	0.6611	1.9953
	yes	no	0.9060	0.2479	0.7349	0.6614	2.0000
	yes	yes	0.8996	0.2457	0.7449	0.7455	1.9971
$W^{s=10}$	yes	yes	0.9030	0.2472	0.7349	0.6725	2.0000
W^{poly_2}	no	no	0.8941	0.2494	0.7517	0.6536	1.9980
	yes	no	0.8944	0.2429	0.7649	0.6556	2.0000
	yes	yes	0.8944	0.2429	0.7649	0.6559	2.0000
ref. diffuse			0.8994	0.2503	0.7960	0.6684	1.9760
ref. sharp			0.9154	0.2502	0.7313	0.6901	2.0000

Table 2: Benchmark values for the second benchmark proposed in [Hysing et al., 2009]. Here y_c denotes the center of mass at time $t = 2$, $v_{\max}$ denotes the maximum rising velocity that appears at time $t_{v_{\max}}$, and $c_{\min}$ denotes the minimal circularity that appears at time $t_{c_{\min}}$. See [Hysing et al., 2009] for the definition of these values. As reference we choose the results from the 3rd group participating in [Hysing et al., 2009] (ref. sharp) and for model 3 in [Aland and Voigt, 2012] (ref. diffuse, $\epsilon = 0.02$).

4.2.1 Setup

In Figure 1 the initial configuration is shown and Table 3 lists the properties of our simulations. The fluid properties are chosen to be similar to the first rising bubble test case in [Hysing et al., 2009]. A liquid droplet with radius $r_0 = 0.25$ is placed at (0, 1.5) on a smooth, solid surface with an initial contact angle of $90°$ in a 0.5×2.0 rectangular domain. The inclination angle of the plate is $45°$. The density of the droplet is greater than that of the surrounding fluid. We have no-slip boundary conditions for the velocity on the left and right side and free-slip on the top side. The conditions (6) and (7) are applied on the bottom solid surface, see Figure 1. The separate and combined influence of the boundary conditions (6) and (7) on the sliding droplets are examined by varying the static contact angle θ, the relaxation factor r and the slip coefficient l, see the fourth to sixth column in Table 4. We vary the contact angle from superhydrophilic to superhydrophobic [Law, 2014]. We initialize the simulations by solving the Cahn-Hilliard equations without convection and a contact angle of $90°$ until a steady state is reached. In total, we perform 21 distinct simulations using the three schemes from Section 3 with W^{poly2} and W^s with $s = 100$, and one additional simulation with $s = 10$ for the fully linear and stabilized scheme with W^s, see the first three columns in Table 4.

Remark 10 (Choice of r and l)**.** *For meaningful values of the relaxation parameter r and the slip coefficient l, we write* (6) *and* (7) *in non-dimensionalized*

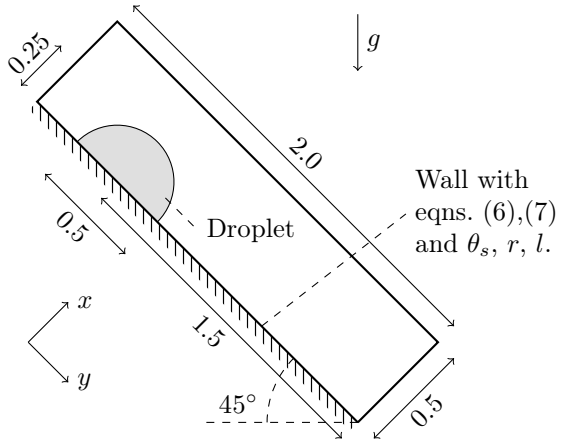

Figure 1: Initial configuration for the sliding droplet simulations.

σ_{12}	ρ_l	ρ_g	η_l	η_g	g	Re	Eo	Ca	A
24.5	1000	100	10	1	-0.98	35	10	0.28	0.81
ϵ	b	τ	$h_{\min}$			Cn	Pe		
2×10^{-2}	2×10^{-5}	5×10^{-5}	0.00625			0.04	14		

Table 3: Parameters used in the sliding droplet simulations.

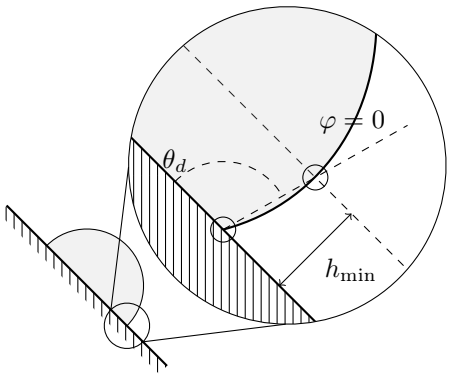

Figure 2: Measurement of the dynamic (or apparent) contact angle.

form,

$$\left[\frac{Ca}{Cn} 2\hat{\eta} D\hat{v}\nu_\Omega + \frac{Ca}{Cn}\frac{L}{l_s} - \hat{L}\hat{\nabla}\varphi\right] \times \nu_\Omega = 0, \tag{31}$$

$$\frac{Ca}{Cn}\frac{r_s}{L}(\partial_{\hat{t}}\hat{\varphi} + \hat{v}\hat{\nabla}\varphi) + \hat{L} = 0, \tag{32}$$

in which $Ca = \eta_l U/\sigma$ *and* $Cn = \epsilon/L$ *are the Capillary number respectively the Cahn number, and* L *and* U *are some characteristic macroscopic length scale respectively velocity. We chose* $r = r_s\eta_l$ *and* $l = \eta_l/l_s$ *such that the dimensionless groups* $\frac{Ca}{Cn}\frac{L}{l_s}$ *and* $\frac{Ca}{Cn}\frac{r_s}{L}$ *are of* $\mathcal{O}(1)$ *[Sibley et al., 2013].*

As benchmark values we again use the three values defined in Section 4.1 with minor modifications, namely for the center of mass, we use a coordinate system that is aligned with the inclined plate, see Figure 1, and for the now called sliding velocity, we use for a the unit vector in tangential direction to the inclined plate. The stretching is used as before.

Additionaly we evaluate two values that are specific for the moving contact line setup. For both the receding and advancing contact line the position of the contact points and a dynamic (or apparent) contact angle measured at some height above the contact points are evaluated. The position of a contact point is defined by

$$y_p = y \text{ on } \partial\Omega \text{ where } \varphi = 0\ , \tag{33}$$

and the dynamic contact angle θ_d is calculated by linear interpolation between y_p and the intersection $y_{p+\Delta}$ where $\varphi = 0$ and $\Delta = h_{\min}$, see Figure 2 and [Omori and Kajishima, 2017].

4.2.2 Results

At first, we reveal the thermodynamic consistency of the schemes by calculating the evolution of the energy inequality using (27). Again, we use γ^{cc} and set $\theta_{eq} =$

150°, $r = 0.35$ and $l = 140$. As one can see from Figure 3, the energy inequality is always fulfilled for all the applied schemes. Note that for $r > 0$ we introduce an additional error as soon as we use the decoupling strategy. In dependence

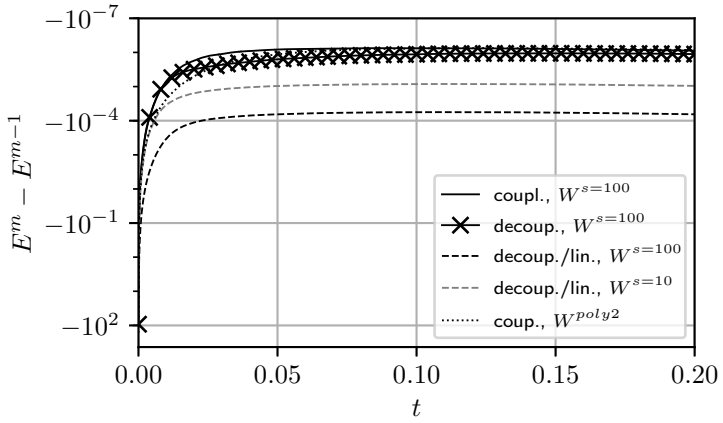

Figure 3: Evolution of the energy inequality (27) for the different schemes. All simulations are performed with γ^{cc}, $\theta_{eq} = 150°$, $r = 0.35$ and $l = 140$.

on θ, r and l the droplets show characteristic developments. The calculated shapes for different combinations of θ_{eq}, r and l at $t = 0.0; 0.5; 1.0; 1.5; 2.0$ are presented in Figure 4. All the simulated droplets show the expected physical behavior: on the hydrophobic surface (third row) the droplet contracts, whereas the droplets spreads on the hydrophilic surface (second row). In addition, the droplets slide down the surface due to the density difference and gravity. The different behavior at the advancing and receding contact points is visible and one can observe nonequilibrium contact angles in the second and third row.

We compare the shapes of the droplets calculated with the different schemes and energy potentials in Figure 4. It is evident, that there are virtually no differences between the coupled (solid black) and decoupled schemes (crosses) for all the contact angles. In contrast, in the linearized scheme with $s = 100$ (dashed black) the dynamics are greatly reduced. Similar as in the rising bubble case, a smaller s ($s = 10$, dashed gray) leads to improvements. For comparison, we show the behavior of the droplet with the coupled scheme and W^{poly2} (dotted line). Here, a slightly different droplet shape is observed especially for later times and large contact angles.

The evolution of the slide velocity v_s, the position of the contact points y_p along the surface and the dynamic contact angle θ_d are displayed in Figure 5. Again, we show all the schemes together with $W^s = 100$ and in addition the stabilized scheme together with $W^s = 10$ and the coupled, nonlinear scheme with W^{poly2}. As expected, in simulations without equilibrium contact angle relaxation ($r = 0$) and slip ($l = 1e6$) (first row) the apparent contact angles on both sides of the droplets stay near the equilibrium value $\theta_{eq} = 90°$ the

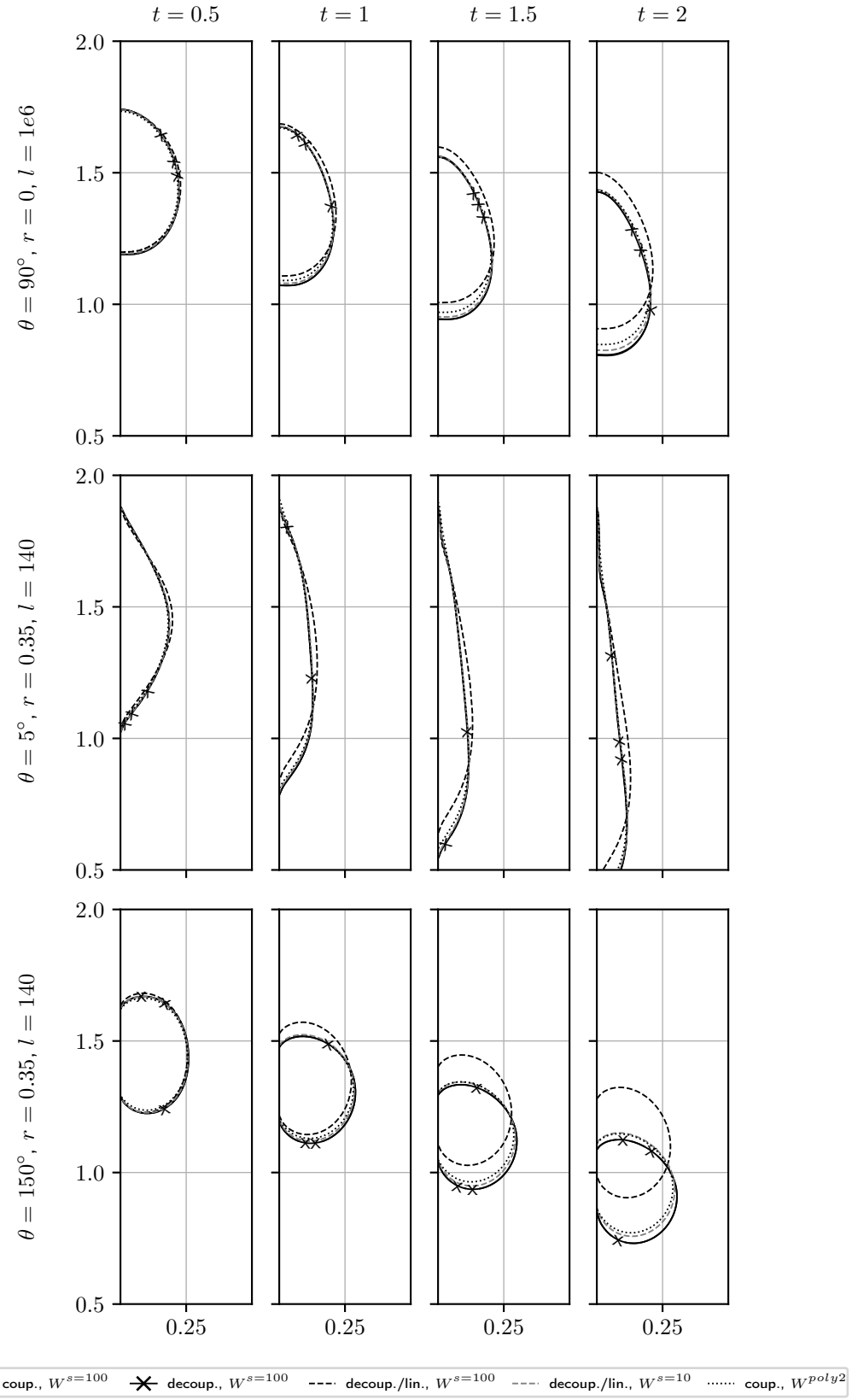

Figure 4: Shapes of the sliding droplets calculated with the schemes from Section 3. Three different surfaces ranging from superhydrophilic (5°, middle) to superhydrophobic (150°, bottom) are compared.

whole time. In contrast, applying the full boundary conditions (6) and (7) with $r = 0.35$ and $l = 140$ leads to clearly visible advancing and receding contact contact angles (third column). To allow for a more quantitative comparison between the solution schemes, we list the characteristic values at $t = 2$ in Table 4. As before, no difference is visible between the coupled (solid black) and decoupled (black crosses) nonlinear schemes for all the characteristic quantities. The characteristic values at $t = 2$ differ only very slightly. The results with the decoupled, stabilized scheme with $s = 100$ (dashed black) are very far off and show very low sliding velocities (left column) and a different contact point behavior (middle column), especially for $\theta_{eq} = 150°$ (last row). The sliding velocities at $t = 2$ differs greatly (around 0.27 for the nonlinear schemes against only 0.20 for the stabilized scheme with $s = 100$). In contrast to the comparison in the bulk only, see Section 4.1, the usage of the coupled scheme with W^{poly2} (dotted black) gives results which are noticeable different from the results with $W^{s=100}$. This is most obvious in the simulations with $\theta_{eq} = 5°$ (middle row): the sliding velocity (left column) is slower and the terminal velocity is reached later. In addition, the receding and advancing contact angles are both lower than in the simulations with $W^{s=100}$. For example, at $t = 2$, the advancing contact angles for W^{poly2} is around 12° smaller than in the nonlinear simulations with $W^{s=100}$.

5 Conclusion

We compare the quality of the numerical results with three different schemes and two different free energy potentials. For simulations without a moving contact line, we find mostly similar results in the bulk independent of the coupling and linearization. However, the linearization of W^s for large s hinders the dynamics to a great extend but gets better for smaller s. In contrast, in the simulations including moving contact lines, we discover a different behavior: The contact dynamics and wetting calculated with W^s and W^{poly2} expressed through the position of the contact line and an apparent contact angle are highly different. Further, we observe, that using the energy stable linear schemes for the bulk energy has a rather large influence on the contact line dynamics, while applying a simple and not energy consistent decoupling (for $r > 0$) together with non linear schemes in the bulk has rather no influence. In future research, we focus on the investigation of the influence of the different forms of γ on microscopic, e.g., equilibrium contact angle, and macroscopic results, e.g., apparent contact angles. Furthermore, the solution schemes are applied to research the behavior of droplets sliding on structured or chemically patterned surfaces.

Acknowledgment

The authors thank Marion Dziwnik for helpful discussions on the correct scaling of the contact line surface tensions. The first and third author acknowledge the

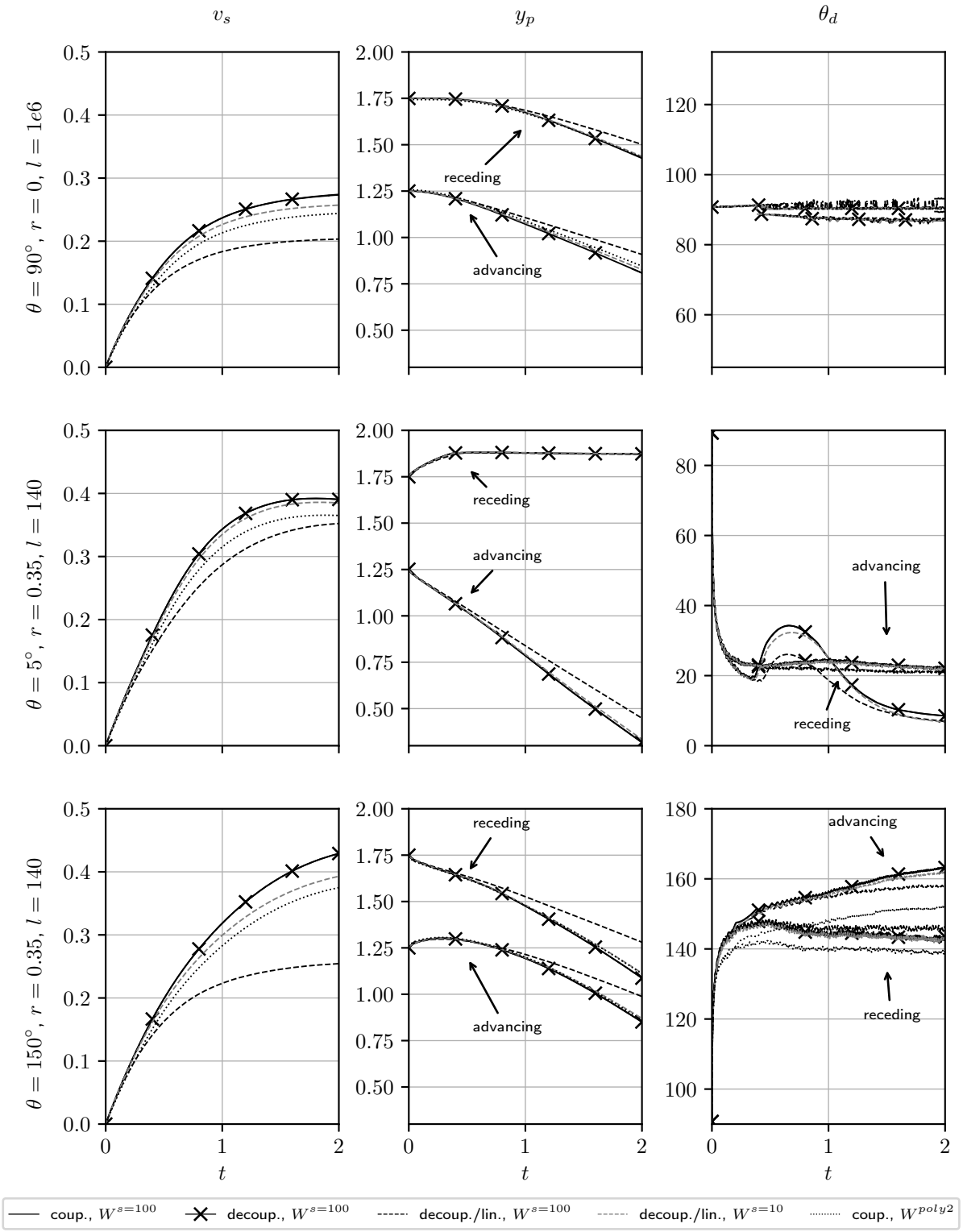

Figure 5: Characteristic quantities calculated with the schemes from Section 3. Three different surfaces ranging from superhydrophilic (5°, middle) to superhydrophobic (150°, bottom) are compared.

Potential	Linear?	Decoup.?	θ_{eq}	r	l	y_c	y_p	v_s	c	θ_d
$W^{s=100}$	no	no				0.9119	0.5699/1.1913	0.2734	0.9499	93.11/89.26
	no	yes				0.9112	0.5717/1.1897	0.2740	0.9523	90.55/86.88
	yes	yes				0.8191	0.4980/1.0917	0.2033	0.9696	90.36/87.25
$W^{s=10}$	yes	yes	90°	0	1×10^6	0.8959	0.5630/1.1731	0.2572	0.9635	90.55/87.06
W^{poly}	no	no				0.8755	0.5678/1.1539	0.2440	0.9640	92.74/89.63
	no	yes				0.8759	0.5684/1.1542	0.2440	0.9642	90.36/87.25
	yes	yes				0.8746	0.5672/1.1526	0.2430	0.9645	90.18/87.25
$W^{s=100}$	no	no				1.0809	0.1268/1.6823	0.3905	0.5162	8.54/22.08
	no	yes				1.0810	0.1265/1.6823	0.3905	0.5162	8.52/22.08
	yes	yes				0.9983	0.1289/1.5517	0.3523	0.5650	6.92/21.12
$W^{s=10}$	yes	yes	5°	0.35	140	1.0693	0.1251/1.6656	0.3849	0.5206	6.72/22.29
W^{poly}	no	no				1.0388	0.1207/1.6412	0.3655	0.5185	9.56/26.56
	no	yes				1.0391	0.0000/0.0000	0.3650	0.5163	0.00/0.00
	yes	yes				1.0364	0.0000/0.0000	0.3632	0.5088	0.00/0.00
$W^{s=100}$	no	no				1.0728	0.9130/1.1494	0.4291	0.8767	163.18/143.41
	no	yes				1.0727	0.9130/1.1493	0.4291	0.8767	163.21/143.41
	yes	yes				0.8878	0.7196/1.0121	0.2544	0.9140	158.24/145.98
$W^{s=10}$	yes	yes	150°	0.35	140	1.0394	0.8858/1.1302	0.3929	0.8937	161.89/142.41
W^{poly}	no	no				1.0133	0.8893/1.1392	0.3751	0.9008	151.84/138.64
	no	yes				1.0132	0.8894/1.1391	0.3749	0.9008	151.88/138.64
	yes	yes				1.0109	0.8855/1.1363	0.3724	0.9014	151.80/138.56

Table 4: Parameters and characteristic values for all the sliding droplets simulations. The inclination angle of the plate is 45° and γ^{cc} is applied as the wall energy. For y_c and c see caption of Table 2. In addition, y_p and θ_d denote the position of the contact points and the dynamic contact angles. The first and second values correspond to the advancing and receding contact point respectively angle. The slide velocity is v_s and all values are reported at $t = 2$.

North-German Supercomputing Alliance (HLRN) for providing HPC resources that have contributed to the research results reported in this paper and thank the German Research Foundation (DFG) for the financial support within the project RE 1705/16-1. The second author gratefully acknowledges the support by the German Research Foundation (DFG) through the International Research Training Group IGDK 1754 “Optimization and Numerical Analysis for Partial Differential Equations with Nonsmooth Structures".

References

[Abels and Breit, 2016] Abels, H. and Breit, D. (2016). Weak Solutions for a Non-Newtonian Diffuse Interface Model with Different Densities. *Nonlinearity*, 29:3426–3453.

[Abels et al., 2013a] Abels, H., Depner, D., and Garcke, H. (2013a). Existence of weak solutions for a diffuse interface model for two-phase flows of incompressible fluids with different densities. *Journal of Mathematical Fluid Mechanics*, 15(3):453–480.

[Abels et al., 2013b] Abels, H., Depner, D., and Garcke, H. (2013b). On an incompressible Navier–Stokes / Cahn–Hilliard system with degenerate mobility. *Annales de l'Institut Henri Poincaré (C) Non Linear Analysis*, 30(6):1175–1190.

[Abels et al., 2012] Abels, H., Garcke, H., and Grün, G. (2012). Thermodynamically consistent, frame indifferent diffuse interface models for incompressible two-phase flows with different densities. *Mathematical Models and Methods in Applied Sciences*, 22(3):1150013(40).

[Aland, 2014] Aland, S. (2014). Time integration for diffuse interface models for two-phase flow. *Journal of Computational Physics*, 262:58–71.

[Aland and Chen, 2016] Aland, S. and Chen, F. (2016). An efficient and energy stable scheme for a phase-field model for the moving contact line problem. *International Journal for Numerical Methods in Fluids*, 81:657–671.

[Aland et al., 2017] Aland, S., Hahn, A., Kahle, C., and Nürnberg, R. (2017). *Comparative Simulations of Taylor Flow with Surfactants Based on Sharp- and Diffuse-Interface Methods*, pages 639–661. Springer International Publishing, Cham.

[Aland and Voigt, 2012] Aland, S. and Voigt, A. (2012). Benchmark computations of diffuse interface models for two-dimensional bubble dynamics. *International Journal for Numerical Methods in Fluids*, 69:747–761.

[Alnæs et al., 2015] Alnæs, M., Blechta, J., Hake, J., Johansson, A., Kehlet, B., Logg, A., Richardson, C., Ring, J., Rognes, M., and Wells, G. (2015). The fenics project version 1.5. *Archive of Numerical Software*, 3(100).

[Amestoy et al., 2001] Amestoy, P. R., Duff, I. S., Koster, J., and L'Excellent, J.-Y. (2001). A fully asynchronous multifrontal solver using distributed dynamic scheduling. *SIAM Journal on Matrix Analysis and Applications*, 23(1):15–41.

[Amestoy et al., 2006] Amestoy, P. R., Guermouche, A., L'Excellent, J.-Y., and Pralet, S. (2006). Hybrid scheduling for the parallel solution of linear systems. *Parallel Computing*, 32(2):136–156.

[Anderson et al., 1998] Anderson, D. M., McFadden, G. B., and Wheeler, A. A. (1998). Diffuse-interface methods in fluid mechanics. *Annu. Rev. Fluid Mech.*, 30(1):139–165.

[Backofen et al., 2018] Backofen, R., Wise, S., Salvalaglio, M., and Voigt, A. (2018). Convexity splitting in a phase field model for surface diffusion. *International Journal of Numerical Analysis and Modeling*.

[Balay et al., 2018a] Balay, S., Abhyankar, S., Adams, M. F., Brown, J., Brune, P., Buschelman, K., Dalcin, L., Eijkhout, V., Gropp, W. D., Kaushik, D., Knepley, M. G., May, D. A., McInnes, L. C., Mills, R. T., Munson, T., Rupp, K., Sanan, P., Smith, B. F., Zampini, S., Zhang, H., and Zhang, H. (2018a). PETSc Web page. `http://www.mcs.anl.gov/petsc`.

[Balay et al., 2018b] Balay, S., Abhyankar, S., Adams, M. F., Brown, J., Brune, P., Buschelman, K., Dalcin, L., Eijkhout, V., Gropp, W. D., Kaushik, D., Knepley, M. G., May, D. A., McInnes, L. C., Mills, R. T., Munson, T., Rupp, K., Sanan, P., Smith, B. F., Zampini, S., Zhang, H., and Zhang, H. (2018b). PETSc users manual. Technical Report ANL-95/11 - Revision 3.9, Argonne National Laboratory.

[Balay et al., 1997] Balay, S., Gropp, W. D., McInnes, L. C., and Smith, B. F. (1997). Efficient management of parallelism in object oriented numerical software libraries. In Arge, E., Bruaset, A. M., and Langtangen, H. P., editors, *Modern Software Tools in Scientific Computing*, pages 163–202. Birkhäuser Press.

[Blowey and Elliott, 1991] Blowey, J. F. and Elliott, C. M. (1991). The Cahn–Hilliard gradient theory for phase separation with non-smooth free energy. Part I: Mathematical analysis. *European Journal of Applied Mathematics*, 2:233–280.

[Bonn et al., 2009] Bonn, D., Eggers, J., Indekeu, J., Meunier, J., and Rolley, E. (2009). Wetting and spreading. *Rev. Mod. Phys.*, 81(2):739–805.

[Caffarelli and Muler, 1995] Caffarelli, L. and Muler, N. (1995). An L^∞ Bound for Solutions of the Cahn–Hilliard Equation. *Archive for Rational Mechanics and Analysis*, 133:129–144.

[Carlson et al., 2012] Carlson, A., Bellani, G., and Amberg, G. (2012). Universality in dynamic wetting dominated by contact-line friction. *Phys. Rev. E - Stat. Nonlinear, Soft Matter Phys.*, 85(4):1–5.

[Colli et al., 2017] Colli, P., Gilardi, G., and Spreckels, J. (2017). On a Cahn–Hilliard system with convection and dynamic boundary conditions. *Annali di Matematica Pura ed Applicata*, pages 1–31.

[Ding and Spelt, 2007] Ding, H. and Spelt, P. (2007). Wetting condition in diffuse interface simulations of contact line motion. *Pysical Review E*, 75:046708.

[Donaldson et al., 2011] Donaldson, A. A., Kirpalani, D. M., and Macchi, A. (2011). Diffuse interface tracking of immiscible fluids: Improving phase continuity through free energy density selection. *Int. J. Multiph. Flow*, 37(7):777–787.

[Eddi et al., 2013] Eddi, A., Winkels, K. G., and Snoeijer, J. H. (2013). Short time dynamics of viscous drop spreading. *Phys. Fluids*, 25(1).

[Garcke et al., 2016] Garcke, H., Hinze, M., and Kahle, C. (2016). A stable and linear time discretization for a thermodynamically consistent model for two-phase incompressible flow. *Applied Numerical Mathematics*, 99:151–171.

[Grün, 2013] Grün, G. (2013). On convergent schemes for diffuse interface models for two-phase flow of incompressible fluids with general mass densities. *SIAM Journal on Numerical Analysis*, 51(6):3036–3061.

[Grün et al., 2016] Grün, G., Guillén-Gonzáles, F., and Metzger, S. (2016). On Fully Decoupled Convergent Schemes for Diffuse Interface Models for Two-Phase Flow with General Mass Densities. *Communications in Computational Physics*, 19(5):1473–1502.

[Grün and Klingbeil, 2014] Grün, G. and Klingbeil, F. (2014). Two-phase flow with mass density contrast: Stable schemes for a thermodynamic consistent and frame indifferent diffuse interface model. *Journal of Computational Physics*, 257(A):708–725.

[Guillén-Gonzáles and Tierra, 2014] Guillén-Gonzáles, F. and Tierra, G. (2014). Splitting schemes for a Navier–Stokes–Cahn–Hilliard model for two fluids with different densities. *Journal of Computational Mathematics*, 32(6):643–664.

[Guillén-González and Tierra, 2013] Guillén-González, F. and Tierra, G. (2013). On linear schemes for a Cahn–Hilliard diffuse interface model. *Journal of Computational Physics*, 234:140–171.

[Hintermüller et al., 2011] Hintermüller, M., Hinze, M., and Tber, M. H. (2011). An adaptive finite element Moreau–Yosida-based solver for a non-smooth Cahn–Hilliard problem. *Optimization Methods and Software*, 25(4-5):777–811.

[Hysing et al., 2009] Hysing, S., Turek, S., Kuzmin, D., Parolini, N., Burman, E., Ganesan, S., and Tobiska, L. (2009). Quantitative benchmark computations of two-dimensional bubble dynamics. *International Journal for Numerical Methods in Fluids*, 60(11):1259–1288.

[Jacqmin, 2000] Jacqmin, D. (2000). Contact-line dynamics of a diffuse fluid interface. *J. Fluid Mech.*, 402(2000):S0022112099006874.

[Kahle, 2017] Kahle, C. (2017). An L^∞ bound for the Cahn–Hilliard equation with relaxed non-smooth free energy density. *International Journal of Numerical Analysis and Modeling*, 14(2):243–254.

[Kay et al., 2008] Kay, D., Styles, V., and Welford, R. (2008). Finite element approximation of a Cahn–Hilliard–Navier–Stokes system. *Interfaces and Free Boundaries*, 10(1):15–43.

[Khatavkar et al., 2006] Khatavkar, V. V., Anderson, P. D., and Meijer, H. E. (2006). On scaling of diffuse-interface models. *Chem. Eng. Sci.*, 61(8):2364–2378.

[Law, 2014] Law, K.-Y. (2014). Definitions for Hydrophilicity, Hydrophobicity, and Superhydrophobicity: Getting the Basics Right. *J. Phys. Chem. Lett.*, 5(4):686–688.

[Logg et al., 2012] Logg, A., Mardal, K.-A., and Wells, G., editors (2012). *Automated Solution of Differential Equations by the Finite Element Method - The FEniCS Book*, volume 84 of *Lecture Notes in Computational Science and Engineering*. Springer.

[Minjeaud, 2013] Minjeaud, S. (2013). An unconditionally stable uncoupled scheme for a triphasic Cahn–Hilliard/Navier–Stokes model. *Numerical Methods for Partial Differential Equations*, 29(2):584–618.

[Omori and Kajishima, 2017] Omori, T. and Kajishima, T. (2017). Apparent and microscopic dynamic contact angles in confined flows. *Phys. Fluids*, 29(11).

[Qian et al., 2006] Qian, T., Wang, X.-P., and Sheng, P. (2006). A variational approach to moving contact line hydrodynamics. *Journal of Fluid Mechanics*, 564:333–360.

[Shen and Yang, 2010] Shen, J. and Yang, X. (2010). A Phase-Field Model and its Numerical Approximation for Two-Phase Incompressible Flows with Different Densities and Viscosities. *SIAM Journal on Scientific Computing*, 32(3):1159–1179.

[Sibley et al., 2013] Sibley, D. N., Nold, A., Savva, N., and Kalliadasis, S. (2013). On the moving contact line singularity: Asymptotics of a diffuse-interface model. *Eur. Phys. J. E*, 36(3).

[Snoeijer and Andreotti, 2013] Snoeijer, J. H. and Andreotti, B. (2013). Moving Contact Lines: Scales, Regimes, and Dynamical Transitions. *Annu. Rev. Fluid Mech.*, 45(1):269–292.

[Yu and Yang, 2017] Yu, H. and Yang, X. (2017). Numerical approximations for a phase-field moving contact line model with variable densities and viscosities. *Journal of Computational Physics*, (334):665–686.